Radial Nanowire Light-Emitting Diodes in the (AlxGa1-x)yIn1-yP Material System

Berg, Alexander; Yazdi, Sadegh; Nowzari, Ali; Storm, Kristian; Jain, Vishal; Vainorius, Neimantas; Samuelson, Lars ; Wagner, Jakob Birkedal; Borgström, Magnus T

Published in:
Nano Letters

Link to article, DOI:
10.1021/acs.nanolett.5b04401

Publication date:
2016

Document Version
Peer reviewed version

Radial nanowire light-emitting diodes in the $(Al_xGa_{1-x})_yIn_{1-y}P$ material system

Alexander Berg,[†] *Sadegh Yazdi,*[‡,⊥] *Ali Nowzari,*[†] *Kristian Storm,*[†] *Vishal Jain,*[†,§] *Neimantas Vainorius,*[†] *Lars Samuelson,*[†] *Jakob B. Wagner,*[‡] *Magnus T. Borgström*[†,*]

[†]Solid State Physics and NanoLund, Lund University, Box 118, SE-221 00, Lund, Sweden

[‡]Center for Electron Nanoscopy, Technical University of Denmark, DK 2800 Kgs. Lyngby, Denmark

[§]Laboratory of Mathematics, Physics and Electrical Engineering, Halmstad University, Box 823, SE-301 18 Halmstad, Sweden

Keywords: Nanowire, radial, quantum well, STEM-EDX, light-emitting diodes, MOCVD

Nanowires have the potential to play an important role for next-generation light-emitting diodes. In this work we present a growth scheme for radial nanowire quantum-well structures in the AlGaInP material system using a GaInP nanowire core as a template for radial growth with GaInP as the active layer for emission and AlGaInP as charge carrier barriers. The different layers were analyzed by x-ray diffraction to ensure

lattice-matched radial structures. Furthermore we evaluated the material composition and hetero-junction interface sharpness by scanning transmission electron microscopy energy dispersive x-ray spectroscopy. The electro-optical properties were investigated by injection luminescence measurements. The presented results can be a valuable track towards radial nanowire light-emitting diodes in the AlGaInP material system in the red/orange/yellow color spectrum.

Nanowires (NWs) are future building blocks for optoelectronic devices such as solar cells,[1] transistors[2] and light-emitting diodes.[3] Due to the small dimensions, NWs can exhibit different electronic and optical properties as compared to planar structures of the same materials. Material combinations that are incompatible in planar structures can be used in NWs, allowing more freedom in bandgap tuning of active segments to desired wavelengths in NW based devices.

It is a common practice in III-As/P planar light-emitting diode structures to use GaInP as the active layer.[4-18] By introducing Al in GaInP, the bandgap can be increased all the way to 2.52 eV in AlP, but which has an indirect bandgap.[19] The Al/Ga ratio in lattice-matched AlGaInP can be tuned to be used as electron blocking layer keeping the (AlGa)/In ratio constant since the lattice constant changes only slightly with increasing Al due to similar lattice constants for AlP and GaP.[19, 20] In planar structures, LEDs based on the AlGaInP material system are often grown on GaAs substrates, since $(Al_xGa_{1-x})_{0.51}In_{0.49}P$ is lattice-matched to GaAs.[19] After synthesis, the GaAs substrate is replaced by a transparent GaP substrate via ”wafer-bonding”.[21-24] Alternatively, in order to grow $Ga_{0.47}In_{0.53}P$ which leads to red light emission[25] on GaP, graded buffer layers are needed to adjust for the 3.6 % lattice mismatch.[19, 20] Graded buffer layers usually

exhibit dislocations which lead to efficiency losses. Therefore the possibility to achieve desired bandgaps is limited. In the NW geometry, the desired composition can be grown directly on substrates with different lattice constants because of the small NW footprint[26, 27] and due to effective strain relaxation via the free surfaces in NWs. For designing radial NW structures lattice matching requirements become more relevant, and the NW core can be used as a "substrate" for growing NW shells that are lattice-matched with the NW core. Radial core-shell NWs have been shown to be a versatile structure for light-emitting diodes[28, 29] because of the larger junction area as compared to axial NW structures. Several contributions on radial NW quantum-well (QW) structures with emission in the infrared (IR) color spectrum based on various material systems have been reported such as GaP/GaAs/GaInP,[30] InP/InAsP/InP,[31, 32] InP/InAs/InP[33, 34] and GaAs/AlGaAs.[35-38] Moreover, radial NW QWs in the short-wavelength visible spectrum with GaN/InGaN/GaN[28, 29, 39] as well as multi-quantum-well (MQW) structures in (In)AlN/GaN[40, 41] emitting in the ultra-violet (UV) region have been reported. Here, we report the growth and characterization of radial NW p-i-n junctions in the AlGaInP material system designed for the long-wavelength visible spectrum. We grow untapered GaInP NW cores on a GaP substrate and use the NW core as a template for radial growth of materials with composition optimized for red light emission. After growing a radial QW structure, the material composition is analyzed, and the effect of different n-type dopant precursors on the growth dynamics is studied. We observe Al enrichment in the corners of the AlGaInP layers in the cross-section perpendicular to the NW axis by use of transmision electron microscopy (TEM). Electrical measurements confirm the presence of a pn-junction and electrical injection results in luminescence in the red color spectrum.

P-doped $(\bar{1}\bar{1}\bar{1})$B GaP wafers were deposited with a 20 nm thick silicon nitride (SiN_x) layer via plasma-enhanced chemical vapor deposition (PECVD). Resist-spinning with a bi-layer method,[42] nanoimprint lithography (IPS/STU process[43]), reactive ion etching (RIE), Au evaporation and lift-off were used to define the template for NW growth. The template consists of a hexagonal pattern of circular holes of 100 nm with a pitch of 1 µm. The deposited Au layer thickness was 10 nm. The material design of the p-type GaInP NW core was reported elsewhere.[44] In short, the core consists of a GaP stub, a GaInP transition segment where the Ga content decreases from p-GaP to p-GaInP of the composition intended for the NW and a long p-GaInP segment with homogenous material composition. The complete radial structure is formed by depositing several additional shell layers on the core: a p-GaInP buffer layer (15 s growth time), a p-AlGaInP cladding layer (30 s), an intrinsic GaInP layer (15 s) as the active layer for carrier recombination, an n-AlGaInP cladding layer (30 s) and an n-GaInP layer (2 min) which is intended to be highly doped for electrical contacts (Figure 1). The p-GaP wafer below the shells is passivated by the SiN_x mask in order to make more precursor material contribute to NW growth and avoid substrate leakage currents from the outermost shell directly into the substrate in device configuration. The NWs were grown by metal-organic chemical vapor deposition (MOCVD) in an Aixtron 200/4 reactor at a pressure of 100 mbar for the core and 50 mbar for the shells. The precursors were trimethylaluminum (TMAl), trimethylgallium (TMG), trimethylindium (TMI), phosphine (PH_3) as well as diethyl zinc (DEZn) for p-type doping and triethyltin (TESn) or hydrogen sulfide (H_2S) for n-type doping, respectively, in a total flow of 13 l/min using hydrogen (H_2) as carrier gas. Hydrogen chloride (HCl) was used to impede radial growth during the synthesis of the NW core.[45-48] The molar fractions for growth of the

p-GaInP segment of the core at 440 °C were χ_{TMG} = 6.724×10^{-5}, χ_{TMI} = 1.228×10^{-5}, χ_{PH3} = 4.6×10^{-3}, χ_{DEZn} = 3.13×10^{-6} and χ_{HCl} = 6.154×10^{-5}. After growth of the NW core with a length of 1.5 µm and cooling the reactor under a PH_3/H_2 mixture, the sample was taken out of the reactor and the gold alloy particle removed by a two-step wet chemical etch process in order to impede catalyzed axial growth during shell growth using H_2SO_4:H_2O (1:10) and KI:I_2:H_2O (4 g : 1 g : 40 ml),[49-51] both for 10 s. After loading the sample back into the reactor, it was heated to 650 °C and the sample was annealed for 4 min under a PH_3/H_2 mixture to remove any oxides on the NW core surface. The shell growth of the different layers, at 650 °C, was initialized/terminated by switching on/off the respective group III and dopant precursor sources. The molar fractions of TMI, PH_3 and DEZn during shell growth were χ_{TMI} = 3.509×10^{-5}, χ_{PH3} = 1.54×10^{-2} and χ_{DEZn} = 3.13×10^{-6}, respectively. For every shell we performed a series of growth experiments on different samples from the same NW core growth run with varying χ_{TMG} for the GaInP shells and a varying sum (χ_{TMAl} + χ_{TMG}) for the AlGaInP shells (but keeping the χ_{TMAl} / (χ_{TMAl} + χ_{TMG}) ratio constant), respectively, in order to achieve lattice-matched compositions between all layers. The molar fractions for TMAl, TMG and the n-type dopants for lattice-matched layers are shown in Table S1. Applying growth parameters for lattice-matched layers using H_2S as n-type dopant, we performed five growth runs with different χ_{TMAl} / (χ_{TMAl} + χ_{TMG}) ratios (but with constant sum (χ_{TMAl} + χ_{TMG})) (Table S2) to evaluate the correlation between the group III precursor molar fractions in the gas phase and the Al concentration in the AlGaInP crystal (Table S2). After shell growth, the sample was cooled down to room temperature under a PH_3/H_2 mixture.

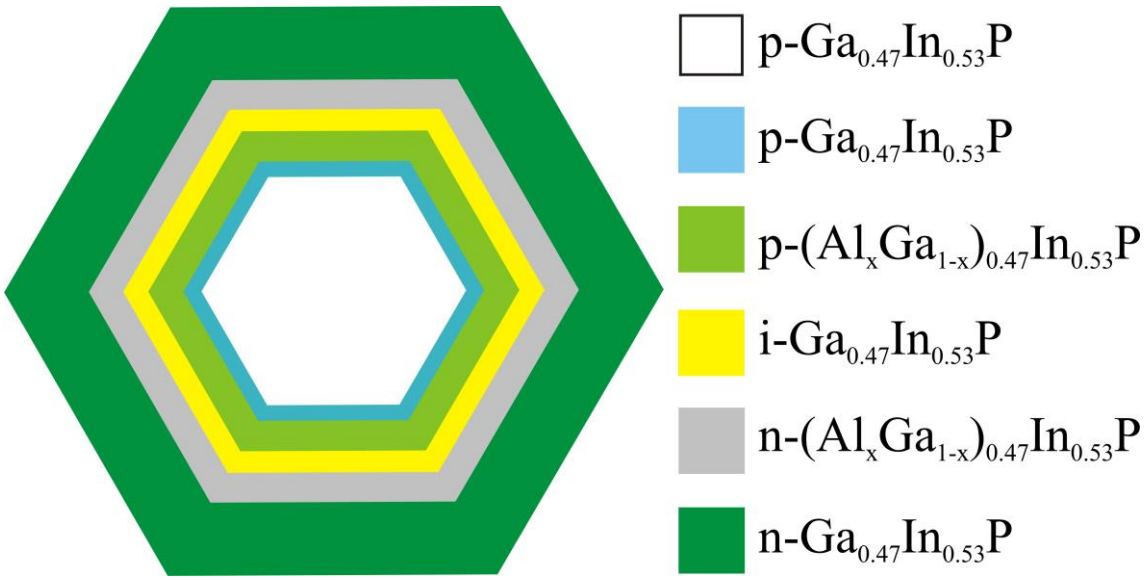

Figure 1. Schematic construction of the grown radial GaInP/AlGaInP/GaInP NWs. The different colors indicate the strain-free layers with desired compositions during the development of the radial structure. The white area in the center is the NW core.

Scanning electron microscopy (SEM) was used to characterize the length, diameter and surface morphology of over 30 NWs in the center of each sample.

In order to determine the ratio between Ga and In in GaInP shells and between (Al+Ga) and In in AlGaInP shells, respectively, x-ray diffraction (XRD) characterization was used. The measurements reveal the composition range in a large amount of NWs from the probed area of the sample corresponding to a few mm^2. Each shell in Figure 1 was characterized individually. After optimization of the p-GaInP shell, the neighboring p-AlGaInP shell was developed according to XRD measurements and so on. Most of these measurements were done during developing a procedure to grow ternary GaInP NW with homogeneous material composition by ramping χ_{TMI} up by 25 % during a growth time of 4 min.[44] Therefore most of the NW cores, except the ones with S-doped n-GaInP shells, had an inhomogeneous composition along the axial

direction of the NW. In order to determine the material composition, the shell under investigation was grown 4-6 times longer than in the final structure in order to get a proper XRD signal from the respective shell which by volume is dominated by the shell under evaluation although it contains the signal from the entire NW (including the broad XRD signal from the NW core). According to Schubert[25] GaInP has a bandgap between 1.65 and 1.99 eV in the red color spectrum, which corresponds to an XRD angle between 27 and 27.4 degrees for 2 Theta for a crystal growing in $(\bar{1}\bar{1}\bar{1})$B direction. For each shell the composition was aimed at $Ga_{0.47}In_{0.53}P$ and $(Al_xGa_{1-x})_{0.47}In_{0.53}P$, respectively, which for GaInP corresponds to a bandgap of 1.82 eV[25] and for the NW core and all shells to an XRD angle 2 Theta of 27.2 degrees.

The NWs were studied by TEM analysis in a probe corrected FEI Titan 80-300 ATEM. Cross-sectional TEM specimens from five samples grown with different χ_{TMAl} / (χ_{TMAl} + χ_{TMG}) ratios in the AlGaInP layers were prepared using focused ion beam (FIB) milling. All the TEM specimens were prepared perpendicular to the axial NW axis of the full core-shell structure (including all layers) in the middle of the axial elongation of the NWs. To study the structure and map the compositional distribution in the NWs, atomic resolution scanning TEM (STEM) and high-angle annular dark-field STEM (HAADF STEM) together with energy dispersive x-ray spectroscopy (EDX) were performed.

In order to optimize the structure for injection luminescence (IL) measurements, we further developed the epitaxial structure. The growth time for the upper segment of the p-GaInP NW core was increased to 6 min to get 1.8-2 µm long NWs and consequently the ramping range for χ_{TMI} increased to about 50 %,[44] which resulted in a ternary p-type $Ga_{0.47}In_{0.53}P$ NW core with homogeneous material composition. On top

158 of the p-GaInP NW core an n-GaP top segment was added in order to avoid leakage
159 from the outermost shell directly into the NW core. The p-GaInP buffer layer
160 (innermost shell) was grown thicker (2 min growth time instead of 15 s) to fill any
161 possible gap between the NW core and SiN_x mask opening and therefore to avoid any
162 current leakage from the QW directly into the substrate. The AlGaInP barriers were
163 grown non-intentionally doped instead of previously p- and n-doped during the
164 development of lattice-matched NW shells. The highest $\chi_{TMAl} / (\chi_{TMAl} + \chi_{TMG})$ ratio of
165 0.63 out of five different growth runs (Table S2) was used to have the highest possible
166 AlGaInP barrier height of our series. Thus the carriers are even more effectively trapped
167 in the QW. For the i-GaInP QW, we made a series of three different growth times (15,
168 30 and 60 s). Preliminary IV-measurements indicated higher rectification ratios using
169 tin (Sn) in the outermost shell as compared to sulphur (S), similar to InP core-shell NW
170 pn-junctions.[50, 52] Therefore we doped the outermost n-GaInP shell with Sn and
171 increased χ_{TESn} to 1.314×10^{-5}.

172 In order to assess the electrical properties of the NWs, 100×100 µm^2 large test
173 LED devices were fabricated. UV lithography and wet etching were used to define the
174 device area and the transparent electrical contacts to the NW shells were fabricated by
175 sputtering indium-tin-oxide (ITO) on the NWs, whereas the NW cores were electrically
176 contacted via the p-type substrate.[52]

177 A probe station was used for measuring IV curves (Figure 4b) at room
178 temperature, whereas IL measurements (Figure 4d) were carried out in another setup - at
179 room temperature as well - in which the outcoming light was collected and measured by
180 a fiber spectrometer. Special care was taken that the relative position between the

detector and the sample was identical for different samples in order to compare the light intensity.

In order to develop a process flow for growing NWs with a radial geometry, it is crucial to design and optimize the growth parameters for each layer in the structure separately. Thereby we analyze the material composition for each layer as a function of group III precursor molar fractions and aim at strain-free NW shells with compositions of $Ga_{0.47}In_{0.53}P$ and $(Al_xGa_{1-x})_{0.47}In_{0.53}P$ for GaInP and AlGaInP layers shown in Figure 1. The p-GaInP buffer layer is used for re-nucleation, in order to overcome any potential surface defects with respect to morphology during wet-etching of the gold alloy particle. XRD measurements show that a crystal composition of $Ga_{0.47}In_{0.53}P$ (XRD angle 2 Theta = 27.2°) can be achieved by tuning χ_{TMG} to 3.812×10^{-5} (Figure 2a). Figure 2b shows the composition of the p-GaInP layer as a function of χ_{TMG} calculated based on XRD measurements.

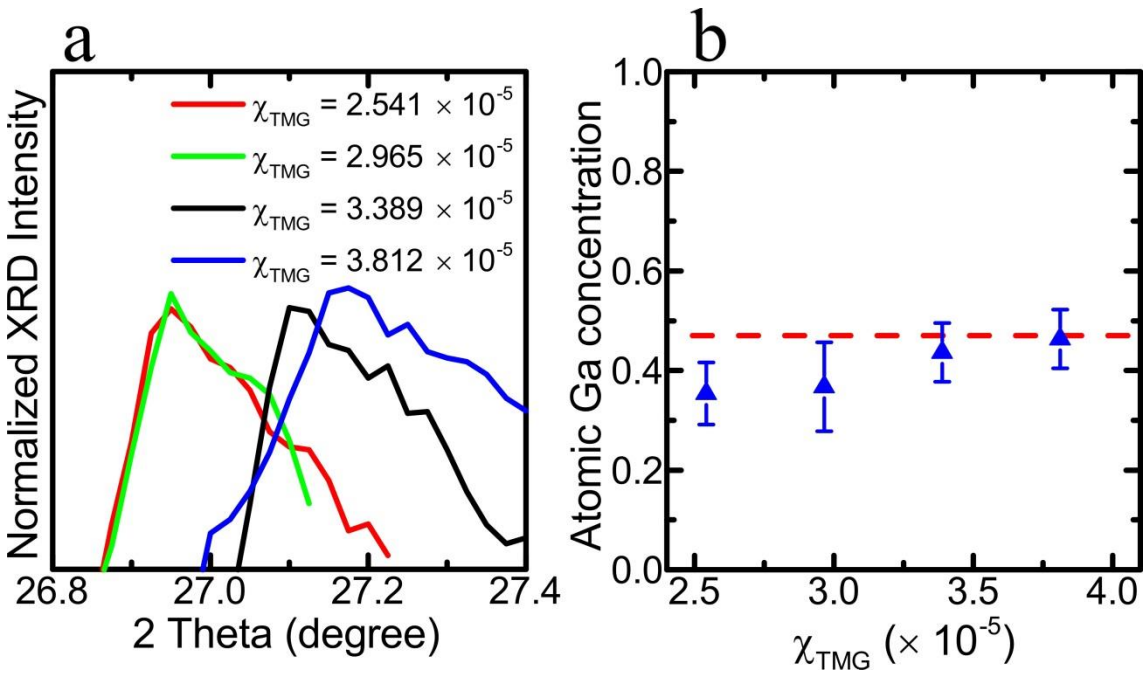

Figure 2. (a) XRD graph for the p-GaInP NW shell layer depending on different χ_{TMG}. 2 Theta was aimed at 27.2° which corresponds to a composition of $Ga_{0.47}In_{0.53}P$. The

197 signal for the two lower molar fractions is cut outside the peak for visibility reasons.
198 The GaP substrate peak is at 28.34°. (b) Atomic Ga concentration for the p-GaInP layer
199 as a function of χ_{TMG}. The error bars indicate the composition range which was
200 determined with the FWHM.[44] The dashed line shows the desired composition
201 $Ga_{0.47}In_{0.53}P$ which corresponds to an XRD 2 Theta degree of 27.2°.
202
203 As stated earlier, most NW cores had an inhomogeneous material composition[44]
204 during the development of lattice-matched shells. Especially for the p-GaInP and p-
205 AlGaInP shell, the composition of the "upper segment" of the core varied from
206 $Ga_{0.3}In_{0.7}P$ to $Ga_{0.44}In_{0.56}P$, which was determined with the full-width-at-half-maximum
207 (FWHM)[44] of the XRD signal for the NW core. Also for the NW shells we observe a
208 broader XRD signal than what is typically observed for completely homogeneous
209 ternary NW materials,[44] which indicates that the NW shell growth also results in an
210 inhomogeneous composition along the axial direction of the NW shell. The growing
211 layer tends to adopt the lattice spacing of the underlying layer and the XRD signal
212 contains all compositions along the axial direction of the NW shells.
213 For the barriers p- and n-AlGaInP we note that AlGaInP can be treated as a
214 combination of AlInP and GaInP. We found out by XRD measurements during
215 optimizing the composition of the p- and n-AlGaInP layers that by adding χ_{TMAl} while
216 keeping the χ_{TMG} and χ_{TMI} at the same value as for the p-GaInP shell, the composition
217 shifts towards a more Al/Ga rich AlGaInP layer as compared to In. Therefore we had to
218 use a lower χ_{TMG} with respect to the previous p-GaInP layer to achieve lattice-matching.
219 If we assume that the Ga and In atoms from the respective precursor molecules are
220 similarly incorporated into AlGaInP as for the p-GaInP layer, then the addition of Al

would by volume result in a higher growth rate. However, we cannot rule out that TMAl reduces the diffusion length of In species, not only dilutes them, and that some Ga atoms are replaced by Al atoms.

The intrinsic GaInP QW layer was grown with the same precursor molar fractions as for the p-GaInP layer since Zn did not affect the composition for shell growth, in agreement with thin-film growth.[53, 54]

For the two n-type layers, two different dopants - Sn and S - were investigated independently of each other. The n-type dopant precursor molar fraction was 6 (5.4) times higher for χ_{TESn} (χ_{H2S}) in the n-GaInP layer than in the n-AlGaInP layer since the outermost layer is intended to be electrically contacted. In case of Sn, χ_{TMAl} and χ_{TMG} had to be reduced by 20 % for the n-AlGaInP layer compared to the p-AlGaInP layer and χ_{TMG} by 11 % for the n-GaInP layer compared to the p- and i-GaInP layers, respectively, in order to achieve lattice-matching. For n-type doping with S, we did not observe any large shift in composition upon doping.

Figure S1 shows the morphology of the n-GaInP outermost shells, doped with Sn (Figure S1a) and S (Figure S1b), respectively, and intrinsic shells for comparison (Figure S1c). The use of TESn leads to the formation of Sn-rich particles on the side facets, similar to n-type shell doping by Sn of GaP[51] and InP[50] core-shell NW pn-junctions. Also for S doping we see several irregularities on the morphology of the surface but the effect is much weaker than for Sn. The NWs with the intrinsic two outermost shells are up to 15 % thicker than the n-type shells doped with Sn or S (not visible in low magnification SEM images in Figure S1), probably because Sn forms a surface accumulation layer[55] and S acts as a surface passivator.[56-58] Table S1 shows the

molar fractions of the precursors during shell growth except for TMI, PH_3 and DEZn (for p-doping) since they were kept constant.

The compositional distribution across the entire NW cross-section, perpendicular to the axial axis of the NWs, was investigated using STEM-EDX. The different radially grown layers are visible in the HAADF STEM image in Figure 3a, where the second highest $\chi_{TMAl} / (\chi_{TMAl} + \chi_{TMG})$ ratio out of five different runs (Table S2) was used. The atomic resolution HAADF image (inset of Figure 3a) shows relatively sharp hetero-interfaces with inter-diffusion of a few atomic layers, indicating no or only small group III intermixing occurs at the hetero-interfaces. The calculated material compositions from the STEM-EDX measurements for each segments across the NW are shown in Figure 3d.

The segments in [110] direction (normal of the "m-plane") are relatively homogeneous in composition with a slight In overweight in the i-GaInP QW layer, close to the intended material compositions $Ga_{0.47}In_{0.53}P$ and $(Al_xGa_{1-x})_{0.47}In_{0.53}P$. However, in [112] direction (in the corners of the hexagon), there are segments with higher Al content in the p- and n-AlGaInP layers which can be seen as black stripes in Figure 3a.

STEM-EDX elemental mapping of the NW composition confirmed Al rich corners in AlGaInP and even Ga rich corners in i- and n-GaInP (Figure 3b). It showed relative radial uniformity only for the p-GaInP buffer layer. Starting from the p-AlGaInP layer towards the outer shells, we observe areas in the six corners in [112] direction with higher Al or Ga contents than in [110] direction. Al aggregates in the corners of the quaternary shells and this phenomenon propagates through to the respective outside lying neighboring shell all the way to the outermost n-GaInP shell. The Ga rich corners in the i- and n-GaInP shells are likely to be formed due to

thermodynamic arguments. The atomic radius of Ga (130 pm) is far closer to the atomic radius of Al (125 pm) than In (155 pm), therefore, for Ga atoms it might be more favorable to deposit next to Al rich corners than next to the AlGaInP facets in [110] direction. In other words, a layer tends to adopt the lattice constant of the neighboring layer upon epitaxial processes. During XRD measurements for the separate layers, we found a relatively broad signal for all shells except for the p-GaInP shell. This could be caused - besides the NW core material composition inhomogeneity in axial direction - by the two different types of segments with different lattice constants in [110] and [112] direction. Al rich vertices of a hexagon have also been observed in other core-shell NW structures such as GaAs/AlInP[59, 60] as well as GaAs/AlGaAs[35-38, 61, 62] and InAlN/GaN/InAlN[40] MQWs.

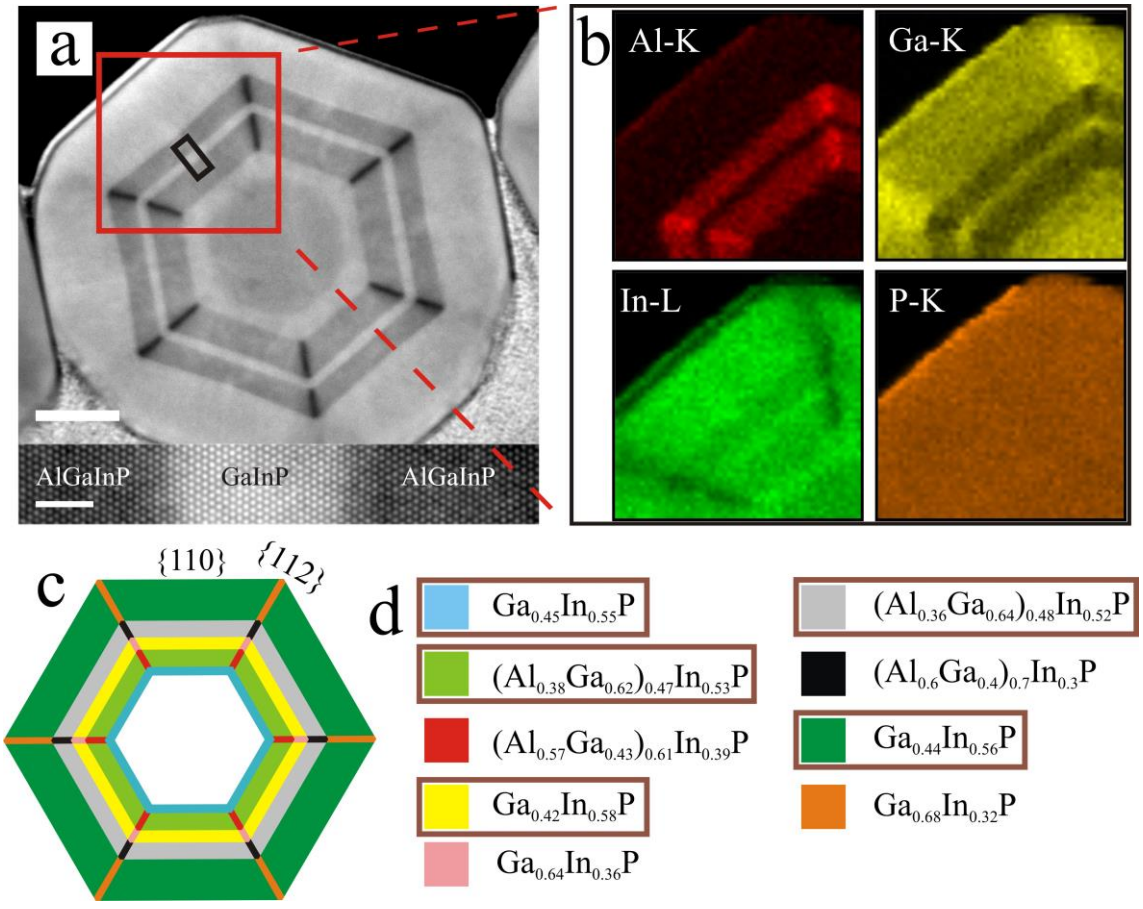

Figure 3. Cross-section images perpendicular to the axial NW axis of radial GaInP/AlGaInP/GaInP core-shell NWs with two AlGaInP layers as barriers where the ratio χ_{TMAl} / (χ_{TMAl} + χ_{TMG}) was 0.55. (a) HAADF STEM image of a FIB-prepared cross-sectional specimen of the whole core-shell NW (the scale bar is 50 nm). The cross-section was taken in the middle of the axial elongation of the NW. The inset shows an atomic resolution STEM image of the GaInP/AlGaInP/GaInP interface from the area in image a marked with a black rectangle (the scale bar in the inset is 2 nm). (b) STEM-EDX maps from the area marked with the red square in the HAADF image, showing the Al, Ga, In and P distribution. (c) schematic cross-section image. The colors indicate different compositions which are calculated in image d. (d) Material composition of different regions of the NW, calculated from the EDX measurements. All segments in [110] direction are nearly lattice-matched and marked with a brown frame.

Sköld *et al.*[59] analyzed Al rich corners in AlInP shells and argued that Al aggregates at the {112} facets because In adatoms have a longer diffusion length than Al adatoms. In adatoms can therefore diffuse away from areas with high surface energies more easily and we believe the same is true here for our quaternary AlGaInP NW shells. Wagner *et al.*[60] derived this phenomenon more in detail using surface curvature where the adatoms diffuse toward the lower chemical potential. Phase segregation has recently also been demonstrated in III-V-V ternary GaAsP core-shell NWs with P enrichment in the corners of the hexagon.[63] The authors argue that the small {112} facets have a curvature-induced high surface chemical potential, which

makes it easier for the group V element arsenic (As) to diffuse away from the {112} facets because of the longer diffusion length of its adatoms.[63]

The fact that the corners of the hexagon are Al/Ga richer as compared to In means that the bandgap of the segments in [112] direction is higher. Thus, carriers will preferably tend to diffuse to the lower-bandgap [110] direction, which means that the lower-bandgap areas become recombination centers. The segments with smaller lattice constants and higher bandgaps do not attract electrons, which would decrease the recombination efficiency by strain-induced non-radiative recombination.

In order to demonstrate the potential of the GaInP/AlGaInP/GaInP core-shell NWs for a radial NW LED, we evaluated their electro-optical properties. The χ_{TMAl} / (χ_{TMAl} + χ_{TMG}) precursor ratio of 0.63 for the AlGaInP barriers (Figure S2) resulted in a barrier height (conduction band offset) of about 118-194 meV (calculated after atomic concentrations from STEM-EDX measurements and refs.[64-66] where $(Al_xGa_{1-x})_yIn_{1-y}P$ lattice-matched to GaAs was used (y=0.51 according to ref.[19])). The series of three different growth times for the i-GaInP QW resulted in thicknesses of 5, 10 and 20 nm (estimated by the STEM image in Figure 3a where the QW thickness was about 5 nm for a growth time of 15 s).

For the 20 nm thick QWs the IL signal from 100×100 μm^2 large devices is relatively weak with a peak at 1.75-1.8 eV (Figure 4a), which corresponds well to a band-to-band electron-hole pair recombination with the bandgap of $Ga_{0.42}In_{0.58}P$ at 1.79 eV[19] where a bowing factor of 0.65 eV for the Γ-band at 300 K was used[19] or 1.75 eV.[25] For thinner QWs we observe a slight blue-shift of the IL peak which we attribute to quantization. For 5 nm QW thickness the peak is broader than for 10 nm, which can be attributed to transitions from the quantized state and the ground state of the conduction

band to the valence band. We find the highest IL intensity for a QW thickness of 10 nm (Figure 4a).

The IV curve in Figure 4b represents the electrical performance of the NW LED device with a 10 nm thick QW. This device has a threshold voltage of approximately 3 V, above which the NW LED starts to emit red light visible to the eye (Figure 4d). The peak intensity increases with the current level (Figure 4c) and does not show any shift in energy. In reverse bias the device shows a current of 17 mA at -3 V until breakdown occurs at about -4 V.

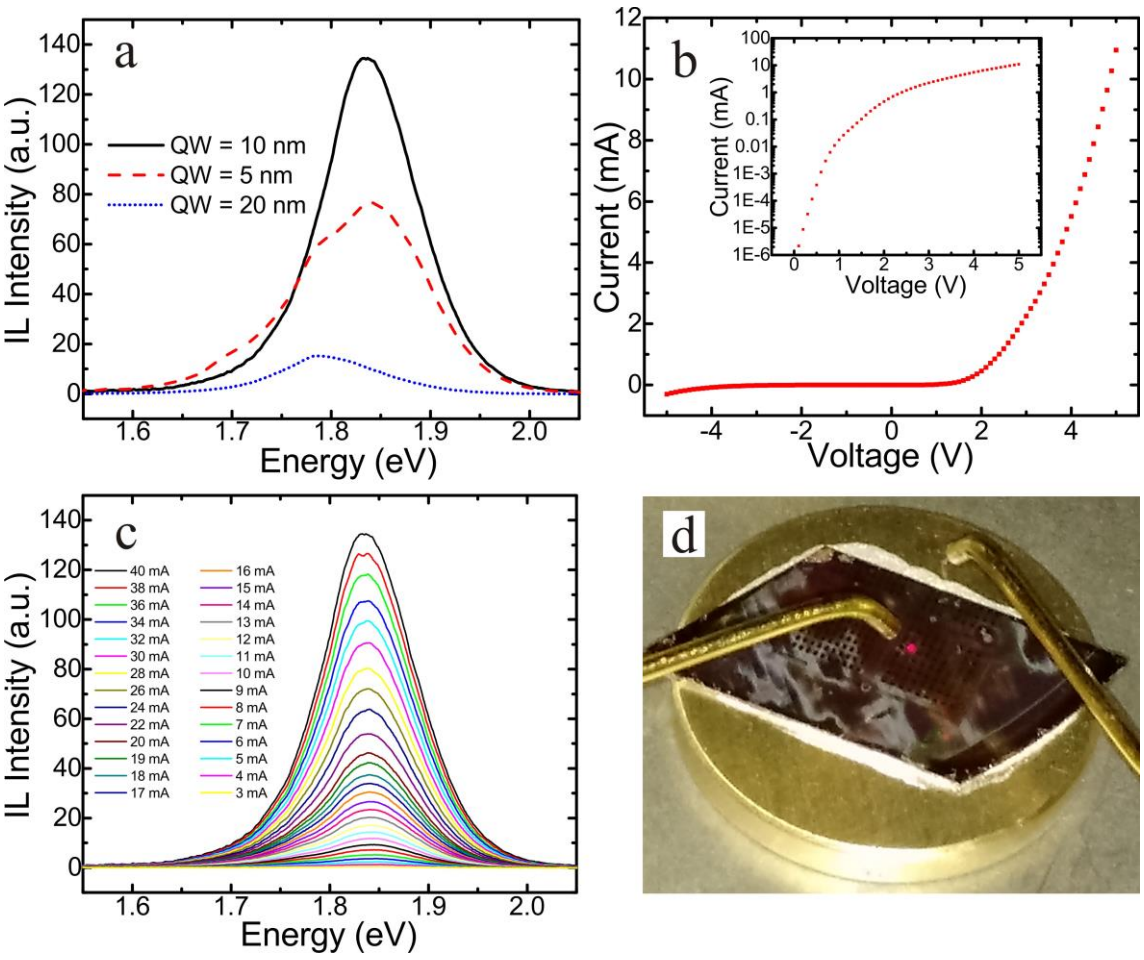

Figure 4. IL measurements on different radial GaInP/AlGaInP/GaInP core-shell NW LED devices. In all 4 images, graphs from the same device with 10 nm QW thickness are shown (image a shows IL spectra of two additional devices). (a) IL spectra of 3

339 devices with different QW thicknesses at 40 mA as a function of the emission energy.
340 (b) IV characteristics. (c) IL spectra for a series of different currents as a function of the
341 energy. (d) photo of the red light emission of the sample in the probe station at a
342 forward bias of about 3 V.

In conclusion, we have presented an epitaxial growth scheme about a radial p-i-n junction nanowire quantum well structure in the AlGaInP material system with GaInP as the active layer. The n-type dopant Sn slightly changes the composition towards In richer material. The material composition of each layer was determined by STEM-EDX. We find Al rich corners in AlGaInP and relate that to a short diffusion length of Al adatoms. Finally we demonstrated the electro-optical properties of the NW light-emitting diode devices. They illuminate with red color at a forward bias of around 3 V.

ASSOCIATED CONTENT

Supporting Information

Additional growth parameters. Morphology of the NW side facets for different n-type dopants. Al content *x* of the p-AlGaInP:Zn and n-AlGaInP:S barriers in $(Al_xGa_{1-x})InP$. PL spectrum of a single NW with 10 nm QW thickness. This material is available free of charge via the Internet at http://pubs.acs.org.

AUTHOR INFORMATION

Corresponding Author

* magnus.borgstrom@ftf.lth.se

Present Address

⊥Department of Materials Science and NanoEngineering, Rice University, 6100 Main Street MS-325, Houston, TX 77005, United States

Author Contributions

The manuscript was written through contributions of all authors. All authors have given approval to the final version of the manuscript.

Notes

The authors declare no competing financial interest.

ACKNOWLEDGMENT

373 This work was performed within NanoLund and supported by the Swedish Research
374 Council (Vetenskapsrådet), the Swedish Foundation for Strategic Research (SSF), by
375 the Knut and Alice Wallenberg Foundation, and by the EU program NWs4Light under
376 grant 280773.

REFERENCES

1. Wallentin, J.; Anttu, N.; Asoli, D.; Huffman, M.; Åberg, I.; Magnusson, M. H.; Siefer, G.; Fuss-Kailuweit, P.; Dimroth, F.; Witzigmann, B.; Xu, H. Q.; Samuelson, L.; Deppert, K.; Borgström, M. T. *Science* **2013,** 339, (6123), 1057-1060.
2. Tomioka, K.; Yoshimura, M.; Fukui, T. *Nature* **2012,** 488, (7410), 189-192.
3. Gudiksen, M. S.; Lauhon, L. J.; Wang, J.; Smith, D. C.; Lieber, C. M. *Nature* **2002,** 415, (6872), 617-620.
4. Wirth, R.; Karnutsch, C.; Kugler, S.; Streubel, K. *Ieee Photonic Tech L* **2001,** 13, (5), 421-423.
5. Sigai, A. G.; Nuese, C. J.; Enstrom, R. E.; Zamerowsi, T. *J Electrochem Soc* **1973,** 120, (7), 947-955.
6. Nuese, C. J.; Sigai, A. G.; Abrahams, M. S.; Gannon, J. J. *J Electrochem Soc* **1973,** 120, (7), 956-965.
7. Nuese, C. J.; Sigai, A. G.; Gannon, J. J.; Zamerowsi, T. *J Electron Mater* **1974,** 3, (1), 51-78.
8. Stinson, L. J.; Yu, J. G.; Lester, S. D.; Peanasky, M. J.; Park, K. *Applied Physics Letters* **1991,** 58, (18), 2012-2014.
9. Kondo, S.; Matsumoto, S.; Nagai, H. *Applied Physics Letters* **1988,** 53, (4), 279-281.
10. Ermakov, O. N.; Garba, L. S.; Golovanov, Y. A.; Sushkov, V. P.; Chukichev, M. V. *Ieee T Electron Dev* **1979,** 26, (8), 1190-1193.
11. Chang, S. J.; Chang, C. S. *Japanese Journal of Applied Physics Part 2* **1998,** 37, (6A), L653-L655.
12. Chang, S. J.; Chang, C. S. *Ieee Photonic Tech L* **1998,** 10, (6), 772-774.
13. Greger, E.; Gulden, K. H.; Riel, P.; Schweizer, H. P.; Moser, M.; Schmiedel, G.; Kiesel, P.; Dohler, G. H. *Applied Physics Letters* **1996,** 68, (17), 2383-2385.
14. Marmalyuk, A. A.; Gorlachuk, P. V.; Ryaboshtan, Y. L.; Brudnyi, V. N.; Prudaev, I. A.; Romanov, I. S.; Lelekov, M. A. *Russ Phys J+* **2013,** 56, (8), 894-897.
15. McGill, L.; Wu, J. W.; Fitzgerald, E. A. *Journal of Applied Physics* **2004,** 95, (12), 7561-7566.
16. Dawson, M. D.; Duggan, G. *Applied Physics Letters* **1994,** 64, (7), 892-894.
17. Lee, C. Y.; Wu, M. C.; Lin, W. *Journal of Crystal Growth* **1999,** 200, (3-4), 382-390.
18. Rooman, C.; Windisch, R.; D'Hondt, M.; Dutta, B.; Modak, P.; Mijlemans, P.; Borghs, G.; Vounckx, R.; Moerman, I.; Kuijk, M.; Heremans, P. *Electron Lett* **2001,** 37, (13), 852-853.
19. Vurgaftman, I.; Meyer, J. R.; Ram-Mohan, L. R. *Journal of Applied Physics* **2001,** 89, (11), 5815-5875.
20. Physical Properties of Semiconductors, Ioffe Institute, Sankt Petersburg, Russia; http://www.ioffe.ru/SVA/NSM/Semicond/.
21. Kish, F. A.; Steranka, F. M.; Defevere, D. C.; Vanderwater, D. A.; Park, K. G.; Kuo, C. P.; Osentowski, T. D.; Peanasky, M. J.; Yu, J. G.; Fletcher, R. M.; Steigerwald, D. A.; Craford, M. G.; Robbins, V. M. *Applied Physics Letters* **1994,** 64, (21), 2839-2841.
22. Höfler, G. E.; Vanderwater, D. A.; DeFevere, D. C.; Kish, F. A.; Camras, M. D.; Steranka, F. M.; Tan, I. H. *Applied Physics Letters* **1996,** 69, (6), 803-805.

23. Gardner, N. F.; Chui, H. C.; Chen, E. I.; Krames, M. R.; Huang, J. W.; Kish, F. A.; Stockman, S. A.; Kocot, C. P.; Tan, T. S.; Moll, N. *Applied Physics Letters* **1999,** 74, (15), 2230-2232.
24. Dakin, J.; Brown, R. G. W., *Handbook of Optoelectronics - Volume I*. Taylor & Francis: New York, 2006.
25. Schubert, E. F., *Light-emitting diodes*. 2nd ed.; Cambridge University Press: Cambridge; New York, 2006.
26. Mårtensson, T.; Svensson, C. P. T.; Wacaser, B. A.; Larsson, M. W.; Seifert, W.; Deppert, K.; Gustafsson, A.; Wallenberg, L. R.; Samuelson, L. *Nano Letters* **2004,** 4, (10), 1987-1990.
27. Roest, A. L.; Verheijen, M. A.; Wunnicke, O.; Serafin, S.; Wondergem, H.; Bakkers, E. P. A. M. *Nanotechnology* **2006,** 17, (11), S271-S275.
28. Qian, F.; Li, Y.; Gradečak, S.; Wang, D. L.; Barrelet, C. J.; Lieber, C. M. *Nano Letters* **2004,** 4, (10), 1975-1979.
29. Qian, F.; Gradečak, S.; Li, Y.; Wen, C. Y.; Lieber, C. M. *Nano Letters* **2005,** 5, (11), 2287-2291.
30. Svensson, C. P. T.; Mårtensson, T.; Tragårdh, J.; Larsson, C.; Rask, M.; Hessman, D.; Samuelson, L.; Ohlsson, J. *Nanotechnology* **2008,** 19, (30), 305201.
31. Kawaguchi, K.; Sudo, H.; Matsuda, M.; Takemoto, K.; Yamamoto, T.; Arakawa, Y. *Applied Physics Letters* **2015,** 106, (1), 012107.
32. Kawaguchi, K.; Sudo, H.; Matsuda, M.; Ekawa, M.; Yamamoto, T.; Arakawa, Y. *Japanese Journal of Applied Physics* **2015,** 54, (4S), 04DN02.
33. Hiruma, K.; Tomioka, K.; Mohan, P.; Yang, L.; Noborisaka, J.; Hua, B.; Hayashida, A.; Fujisawa, S.; Hara, S.; Motohisa, J.; Fukui, T. *Journal of Nanotechnology* **2012,** 2012, 29.
34. Mohan, P.; Motohisa, J.; Fukui, T. *Applied Physics Letters* **2006,** 88, (13), 133105.
35. Mancini, L.; Fontana, Y.; Conesa-Boj, S.; Blum, I.; Vurpillot, F.; Francaviglia, L.; Russo-Averchi, E.; Heiss, M.; Arbiol, J.; Fontcuberta i Morral, A.; Rigutti, L. *Applied Physics Letters* **2014,** 105, (24), 243106.
36. Heiss, M.; Fontana, Y.; Gustafsson, A.; Wust, G.; Magen, C.; O'Regan, D. D.; Luo, J. W.; Ketterer, B.; Conesa-Boj, S.; Kuhlmann, A. V.; Houel, J.; Russo-Averchi, E.; Morante, J. R.; Cantoni, M.; Marzari, N.; Arbiol, J.; Zunger, A.; Warburton, R. J.; Morral, A. F. I. *Nat Mater* **2013,** 12, (5), 439-444.
37. Fickenscher, M.; Shi, T.; Jackson, H. E.; Smith, L. M.; Yarrison-Rice, J. M.; Zheng, C. L.; Miller, P.; Etheridge, J.; Wong, B. M.; Gao, Q.; Deshpande, S.; Tan, H. H.; Jagadish, C. *Nano Letters* **2013,** 13, (3), 1016-1022.
38. Zheng, C. L.; Wong-Leung, J.; Gao, Q.; Tan, H. H.; Jagadish, C.; Etheridge, J. *Nano Letters* **2013,** 13, (8), 3742-3748.
39. Armitage, R.; Tsubaki, K. *Nanotechnology* **2010,** 21, (19), 195202.
40. Durand, C.; Bougerol, C.; Carlin, J. F.; Rossbach, G.; Godel, F.; Eymery, J.; Jouneau, P. H.; Mukhtarova, A.; Butté, R.; Grandjean, N. *Acs Photonics* **2014,** 1, (1), 38-46.
41. Qian, F.; Brewster, M.; Lim, S. K.; Ling, Y. C.; Greene, C.; Laboutin, O.; Johnson, J. W.; Gradecak, S.; Cao, Y.; Li, Y. *Nano Letters* **2012,** 12, (6), 3344-3350.
42. Carlberg, P.; Graczyk, M.; Sarwe, E. L.; Maximov, I.; Beck, M.; Montelius, L. *Microelectron Eng* **2003,** 67-68, 203-207.

43. Eriksson, T.; Yamada, S.; Krishnan, P. V.; Ramasamy, S.; Heidari, B. *Microelectron Eng* **2011,** 88, (3), 293-299.
44. Berg, A.; Lenrick, F.; Vainorius, N.; Beech, J. P.; Wallenberg, L. R.; Borgström, M. T. *Nanotechnology* **2015,** 26, (43), 435601.
45. Borgström, M. T.; Wallentin, J.; Trägårdh, J.; Ramvall, P.; Ek, M.; Wallenberg, L.; Samuelson, L.; Deppert, K. *Nano Research* **2010,** 3, (4), 264-270.
46. Berg, A.; Lehmann, S.; Vainorius, N.; Gustafsson, A.; Pistol, M.-E.; Wallenberg, L. R.; Samuelson, L.; Borgström, M. T. *Journal of Crystal Growth* **2014,** 386, (0), 47-51.
47. Jacobsson, D.; Persson, J. M.; Kriegner, D.; Etzelstorfer, T.; Wallentin, J.; Wagner, J. B.; Stangl, J.; Samuelson, L.; Deppert, K.; Borgström, M. T. *Nanotechnology* **2012,** 23, (24), 245601.
48. Assali, S.; Zardo, I.; Plissard, S.; Kriegner, D.; Verheijen, M. A.; Bauer, G.; Meijerink, A.; Belabbes, A.; Bechstedt, F.; Haverkort, J. E. M.; Bakkers, E. P. A. M. *Nano Letters* **2013,** 13, (4), 1559-1563.
49. Green, T. A. *Gold Bull* **2014,** 47, (3), 205-216.
50. Heurlin, M.; Hultin, O.; Storm, K.; Lindgren, D.; Borgström, M. T.; Samuelson, L. *Nano Letters* **2014,** 14, (2), 749-753.
51. Yazdi, S.; Berg, A.; Borgström, M. T.; Kasama, T.; Beleggia, M.; Samuelson, L.; Wagner, J. B. *Small* **2015,** 11, (22), 2687-2695.
52. Nowzari, A.; Heurlin, M.; Jain, V.; Storm, K.; Hosseinnia, A.; Anttu, N.; Borgström, M. T.; Pettersson, H.; Samuelson, L. *Nano Letters* **2015,** 15, (3), 1809-1814.
53. Lee, S. H.; Fetzer, C. M.; Stringfellow, G. B.; Choi, C. J.; Seong, T. Y. *Journal of Applied Physics* **1999,** 86, (4), 1982-1987.
54. Wu, M. C.; Su, Y. K.; Chang, C. Y.; Cheng, K. Y. *Journal of Applied Physics* **1985,** 58, (11), 4317-4321.
55. Clawson, A. R.; Hanson, C. M. *J Electron Mater* **1991,** 20, (5), 365-372.
56. Hou, X. Y.; Cai, W. Z.; He, Z. Q.; Hao, P. H.; Li, Z. S.; Ding, X. M.; Wang, X. *Applied Physics Letters* **1992,** 60, (18), 2252-2254.
57. Ohno, T. *Phys Rev B* **1991,** 44, (12), 6306-6311.
58. Tian, S. S.; Wei, Z. P.; Li, Y. F.; Zhao, H. F.; Fang, X.; Tang, J. L.; Fang, D.; Sun, L. J.; Liu, G. J.; Yao, B.; Ma, X. H. *Mat Sci Semicon Proc* **2014,** 17, 33-37.
59. Sköld, N.; Wagner, J. B.; Karlsson, G.; Hernan, T.; Seifert, W.; Pistol, M. E.; Samuelson, L. *Nano Letters* **2006,** 6, (12), 2743-2747.
60. Wagner, J. B.; Sköld, N.; Wallenberg, L. R.; Samuelson, L. *Journal of Crystal Growth* **2010,** 312, (10), 1755-1760.
61. Rudolph, D.; Funk, S.; Doblinger, M.; Morkötter, S.; Hertenberger, S.; Schweickert, L.; Becker, J.; Matich, S.; Bichler, M.; Spirkoska, D.; Zardo, I.; Finley, J. J.; Abstreiter, G.; Koblmüler, G. *Nano Letters* **2013,** 13, (4), 1522-1527.
62. Jiang, N.; Gao, Q.; Parkinson, P.; Wong-Leung, J.; Mokkapati, S.; Breuer, S.; Tan, H. H.; Zheng, C. L.; Etheridge, J.; Jagadish, C. *Nano Letters* **2013,** 13, (11), 5135-5140.
63. Zhang, Y.; Sanchez, A. M.; Wu, J.; Aagesen, M.; Holm, J. V.; Beanland, R.; Ward, T.; Liu, H. *Nano Letters* **2015,** 15, (5), 3128-3133.
64. Meney, A. T.; Prins, A. D.; Phillips, A. F.; Sly, J. L.; Oreilly, E. P.; Dunstan, D. J.; Adams, A. R.; Valster, A. *Ieee J Sel Top Quant* **1995,** 1, (2), 697-706.
65. Yow, H. K.; Houston, P. A.; Hopkinson, M. *Applied Physics Letters* **1995,** 66, (21), 2852-2854.

519 66. Zhang, X. H.; Chua, S. J.; Fan, W. J. *Applied Physics Letters* **1998,** 73, (8),
520 1098-1100.
521
522
523 **Table of Contents Graphic**
524

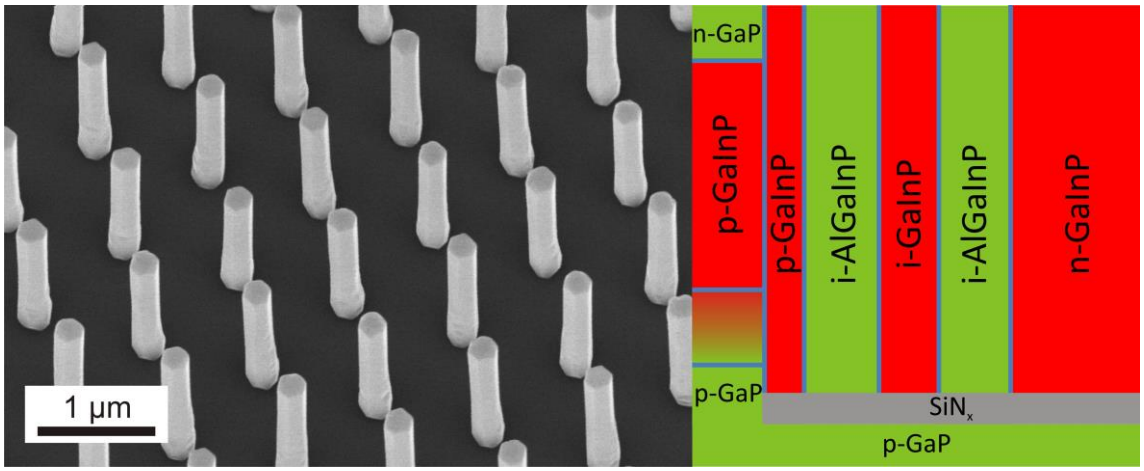

525